Probing the nature of the pre-merging system Hickson Compact Group 31 through integral field unit data[⋆]

M. Alfaro-Cuello,[1]† S. Torres-Flores,[1]† E. R. Carrasco,[2]† C. Mendes de Oliveira,[3] D. F. de Mello[4] and P. Amram[5]

[1]*Departamento de Física y Astronomía, Universidad de La Serena, Av. Cisternas 1200, La Serena, Chile*
[2]*Gemini Observatory/AURA, Southern Operations Center, Casilla 603, La Serena, Chile*
[3]*Instituto de Astronomia, Geofísica e Ciências Atmosféricas da Universidade de São Paulo, Cidade Universitária, CEP:05508-900, São Paulo, SP, Brazil*
[4]*Catholic University of America, Washington, DC 20064, USA*
[5]*Aix Marseille Université, CNRS, Laboratoire d'Astrophysique de Marseille, France*

ABSTRACT

We present a study of the kinematics and the physical properties of the central region of the Hickson Compact Group 31 (HCG 31), focusing on the HCG 31A+C system, using integral field spectroscopy data taken with the Gemini South Telescope. The main players in the merging event (galaxies A and C) are two dwarf galaxies, which have had one close encounter, given the observed tidal tails, and may now be in their second approach, and are possibly about to merge. We present new velocity fields and Hα emission, stellar continuum, velocity dispersion, electron density, Hα equivalent-width and age maps. Considering the high spatial resolution of the integral field unit data, we were able to measure various components and estimate their physical parameters, spatially resolving the different structures in this region. Our main findings are the following: (1) We report for the first time the presence of a super stellar cluster next to the burst associated with the HCG 31C central blob, related to the high values of velocity dispersion observed in this region as well as to the highest value of stellar continuum emission. This may suggest that this system is cleaning its environment through strong stellar winds that may then trigger a strong star formation event in its neighbourhood. (2) Among other physical parameters, we estimate $L(\mathrm{H}\alpha) \sim 14 \times 10^{41}$ erg s^{-1} and the star formation rate, SFR $\sim$11 M$_\odot$ yr^{-1} for the central merging region of HCG 31A+C. These values indicate a high star formation density, suggesting that the system is part of a merging object, supporting previous scenarios proposed for this system.

Key words: galaxies: interactions – galaxies: kinematics and dynamics – galaxies: starburst.

1 INTRODUCTION

Local compact groups of galaxies are excellent for studying galaxy transformation. As a consequence of the strong gravitational

encounters, galaxies in compact groups develop tidal tails, bursts of star formation, gas flows, nuclear activity and kinematic perturbations. All these phenomena have strong influences on the evolution of galaxies in compact groups. For example, simulations suggest the existence of gas inflows in merging systems. These flows can mix the metal content of the interacting galaxies (Rupke, Kewley & Barnes 2010; Perez, Michel-Dansac & Tissera 2011), and can enhance the star formation of the central parts of the interacting/merging systems, increasing their infrared (IR) luminosities. On the other hand, such interactions can affect the global kinematics of the galaxies in the compact group. This effect can be easily seen in the 2D velocity fields of such systems (Amram et al. 2003; Plana et al. 2003). Given that all the phenomena listed above are connected, it will be desirable to analyse all of them simultaneously, which in practice is not an easy task, given the lack of proper data and instrumental limitations. A way to circumvent some of these

limitations is to use integral field unit (IFU) spectroscopic data, given that this technique allows us to observe simultaneously the spectra of several regions, if the galaxy configuration is compact enough. We have IFU observations of one of the most interesting compact groups of galaxies: Hickson Compact Group 31 (HCG 31, Hickson 1982). We can use these to study the evolutionary phase of this group and to search for a link between its kinematics and chemical enrichment history. In addition, this system is an ideal laboratory for studying star formation at different levels (from small to giant star-forming regions), therefore, IFU data for HCG 31 will be extremely useful for understanding the star formation process in interacting and merging galaxies.

HCG 31 is an intriguing object because of its wide range of indicators of galaxy interaction and merging, like multiple tidal tails, irregular morphology, complex kinematics, strong starburst spots and the possible formation of tidal dwarf galaxies (Rubin, Hunter & Ford 1990; López-Sánchez, Esteban & Rodríguez 2004; Mendes de Oliveira et al. 2006; Amram et al. 2007). HCG 31 is formed from several members: A+C, B, E, F, G, H, Q and R (Mendes de Oliveira et al. 2006). Galaxies A and C form the main central part. These are late-type gas-rich large Magellanic-type irregular galaxies (Amram et al. 2007), which could be responsible for the two optical tidal tails that extend towards the north-east and south-west of the A+C system. In addition, tidal dwarf galaxy candidates seem to have been formed out of gas-rich material stripped from this system (López-Sánchez et al. 2004). Two scenarios have been proposed to explain the nature of the system A+C: it is a single entity, i.e., a single interacting galaxy (Richer et al. 2003) or there are two systems in a merging process (Rubin et al. 1990). This latter scenario is supported by Amram et al. (2007), who found that the dynamics of the A+C system has two main components of approximately the same intensities, indicating that it is in a pre-merging stage.

In this paper, we present integral field spectroscopic observations of the central region of HCG 31. We describe the Gemini integral field spectroscopic observations, data reductions and analysis in Sections 2 and 3, respectively. Our results are presented in Section 4. The discussion and conclusions are presented in Sections 5 and 6, respectively. We have adopted a distance of 57.6 Mpc assuming a redshift $z = 0.0137$ (Hickson et al. 1992) and $H_0 = 72 \, \mathrm{km \, s^{-1} \, Mpc^{-1}}$.

2 OBSERVATIONS AND DATA REDUCTION

The central region of HCG 31 was observed with the Gemini South telescope during the nights of 2013 January 12–19, with the Gemini Multi-Object Spectrograph (GMOS, Hook et al. 2004) and the IFU (Allington-Smith et al. 2002), under the program GS-2012B-Q-60 (PI S. Torres-Flores). To get a larger spatial coverage and to map the whole A+C system, three different fields were observed with the IFU in two-slit mode. The spectra and calibrations were acquired using the grating R400+r′-filter centred at 6300 Å. In the two-slit mode, the IFU covers a field of view of 7 × 5 arcsec. Each IFU hexagonal element (the two-slit mode uses 1500 elements) has a projected scale of 0.2 arcsec on the sky. For each field, three exposures of 700 s each were obtained (no spectral or spatial dithering was applied during the observations). All fields were observed during dark time (sky background 50 per cent) at an airmass between 1.23 and 1.31, with median seeing values of ∼0.5 arcsec and 0.6 arcsec and were not taken under photometric conditions (cloud cover 70 per cent cirrus). Fig. 1 shows an *Hubble Space Telescope* (*HST*) optical image [Advanced Camera for Surveys (ACS), F435W] with the location of the three GMOS/IFU fields superimposed on to it (east, centre and west fields, respectively). In addition, the spectropho-

metric standard star LTT 4364 was observed on 2013 January 15 to flux-calibrate the science spectrum.

The observations were processed using a modified early version of the Gemini/GMOS IRAF package to reduce IFU spectra.[1] A master bias was generated from combined raw bias frames. Then all science exposures, comparison lamps, spectroscopic twilight flats and Gemini Calibration Unit lamp flats (GCAL flats) were overscanned and trimmed, and the bias subtracted using the master bias. Identification of fibres was performed with the task GFREDUCE using high signal-to-noise GCAL flats. The resulting file with the fibre identifications was used later as a reference to identify the fibres in the comparison lamps, science exposures and spectroscopic twilight flats. The GCAL flats were processed by removing the GCAL+GMOS spectral response and the uneven illumination introduced by the GCAL unit. The twilight flats were used to determine the relative fibre throughput and to correct for any illumination pattern in the GCAL flat using the GFRESPONSE task. Calibration by wavelength was done using a high signal-to-noise CuAr comparison lamp using the GSWAVELENGTH routine. The residual values in the wavelength solution typically yielded a rms of ∼0.1 Å. The science exposures were then flat-fielded, corrected by the relative fibre throughput, the wavelengths were calibrated, and the sky subtracted and extracted. The same reduction steps were applied to process the standard star LTT 4364. The sensitivity function was derived using the GSSTANDARD routine and the science exposures were then flux-calibrated using the routine GSCALIBRATE.

The final step was the construction of data cubes for further analysis. Each processed 2D science image was transformed to a 3D data cube (x, y, λ) using the GFCUBE routine. The output data cubes (three per field) were re-sampled to square pixels 0.1 arcsec in size and corrected for atmospheric differential refraction. To produce a single data cube for each field, the three cubes were combined using the program PYMOSAIC kindly provided by Dr James Turner (2013, private communication). The final spectra have a resolution of ∼2.4 s in full width at half-maximum (FWHM; measured using the sky line at 6300 Å) and a dispersion of ∼0.68 Å pix^{-1}, covering a wavelength interval of ∼5620–6980 Å.

3 ANALYSIS

The optical emission of the central region of HCG 31A+C is dominated by two main bursts of star formation, which coincide with the centres of galaxies HCG 31A and HCG 31C (Iglesias-Páramo & Vílchez 1997). The ages of these bursts are very similar and therefore it is inferred that they were triggered by the interaction between galaxies A and C (Iglesias-Páramo & Vilchez 1997). López-Sánchez et al. (2004) detected some underlying stellar emission associated with these bursts. However, it is negligible compared with the strong emission from the nebular lines. In this work, we will focus on the flux from the ionized gas. In Fig. 2, we show a typical spectrum observed for the central region of HCG 31A+C. This spectrum is dominated by strong emission lines, where the line ratios are typical of star-forming regions in the BPT plot (Baldwin, Phillips & Terlevich 1981), with almost no emission from an underlying stellar population.

Fig. 3 is an optical image for *HST*/ACS (F435W) for the system HCG 31A+C. We have overplotted the three IFU fields in red rectangles (5 × 7 arcsec or ∼1355 × 1897 pc each). In

---

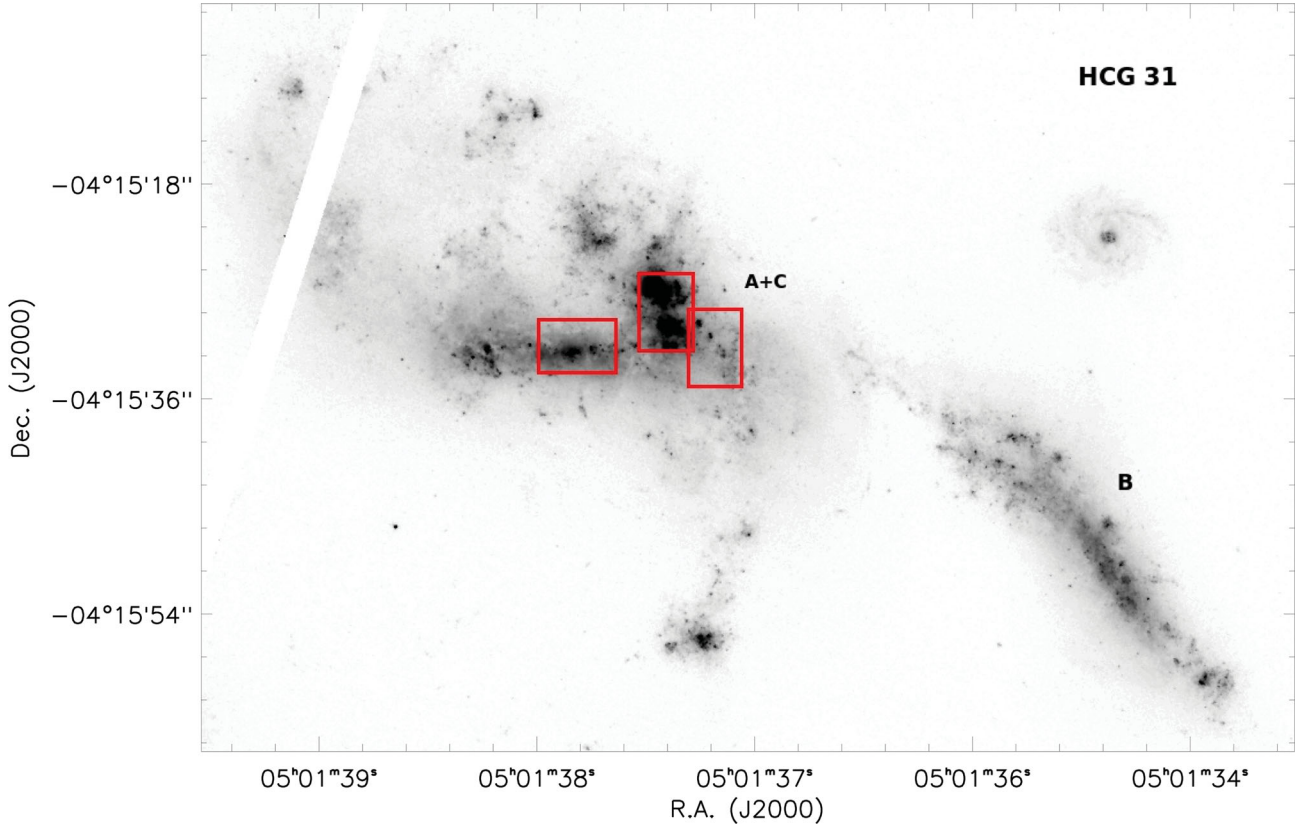[1] http://drforum.gemini.edu/topic/gmos-ifu-data-reduction-scripts/

Figure 1. *Hubble Space Telescope* (HST) optical image (ACS, F435W) of regions A+C, B and part of the south-east tidal tail of HCG 31. The red squares show the location of the three IFUs in the region A+C. These regions are denominated, from left to right: east, centre and west. Image published by Torres-Flores et al. (2015, reproduced by permission of the AAS).
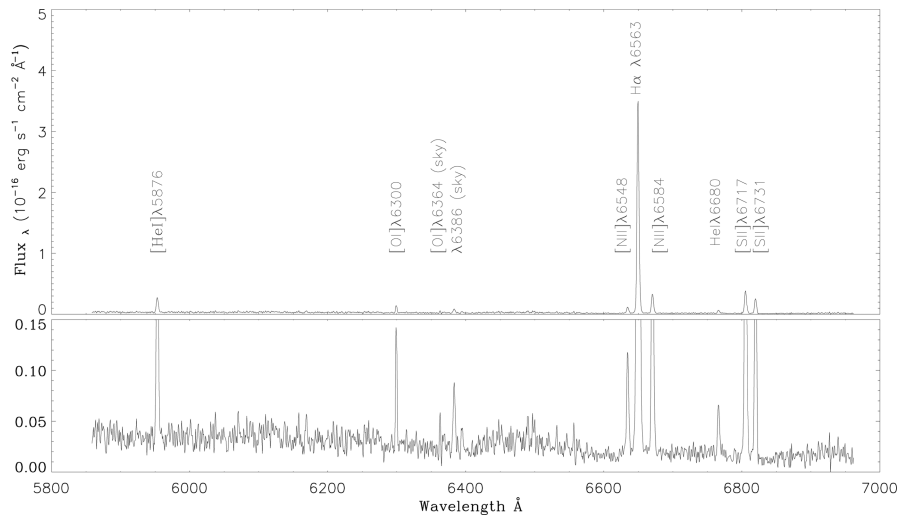

Figure 2. Top spectrum: An example of the typical spectrum observed for the central region of HCG 31. The main emission lines are labelled on this image. The position of the region that has this spectrum is shown in Fig. 1 (5 × 7 arcsec centred on RA 5^{h}1^{m}37^s.77, Dec. −4 ° 15′30′′.24). Bottom spectrum: Zoom of the continuum emission of the top spectrum.

addition, we have overplotted the position of the two main bursts of star formation detected by Iglesias-Páramo & Vílchez (1997) in yellow squares, which are located in the galaxies HCG 31C and HCG 31A (boxes have sizes 1.1 × 1.1 arcsec or ∼298 × 298 pc). The box size was chosen by considering the burst associated with the galaxy HCG 31C, since this burst shows a stronger and more extended Hα emission. The mean values of the different physical

parameters of these two main bursts were obtained considering this area.

3.1 Extinction

The observed flux should be affected by Galactic and internal extinction. We corrected the observed flux for Galactic extinction
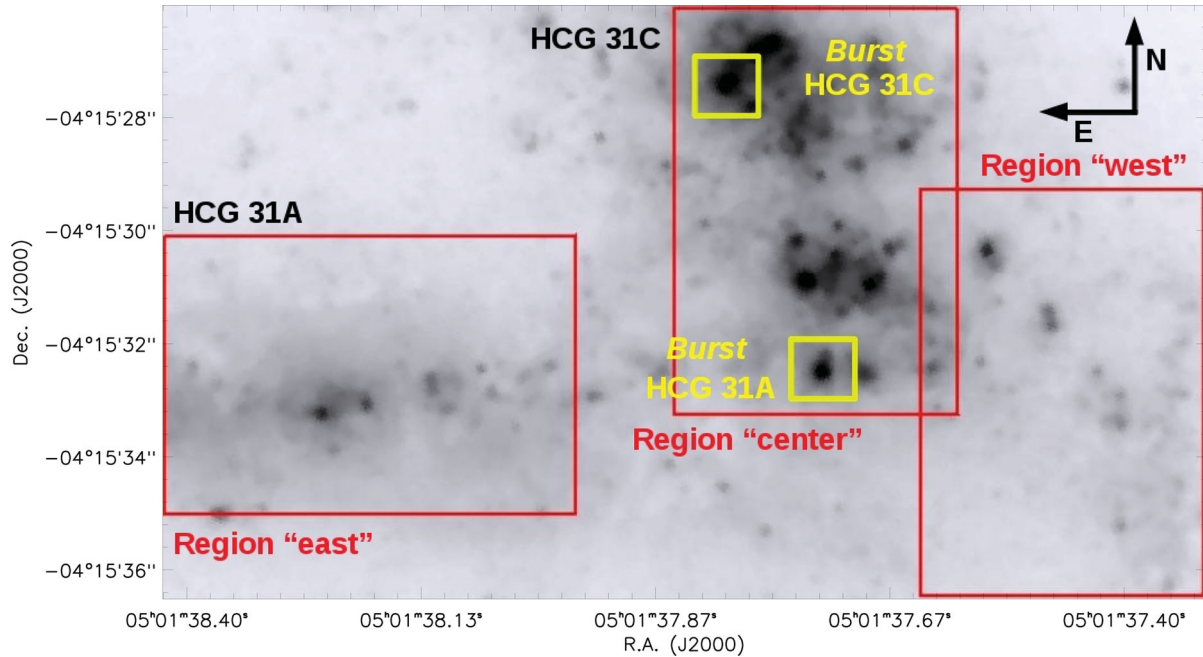
Figure 3. *Hubble Space Telescope* (*HST*) optical image (ACS, F435W) of the system HCG 31A+C. Regions east, centre and west each have a field of view 5×7 arcsec. Red boxes indicate the position of the observed IFUs also shown in Fig. 1. Yellow boxes show the positions of the two main bursts. The northern burst is associated with the galaxy HCG 31C and the southern burst with galaxy HCG 31A. Each box has an area of 1.1×1.1 arcsec ($\sim 298 \times 298$ pc).

using a colour excess of $E(B - V) = 0.04$ mag (NASA/IPAC Extragalactic Database)[2] and the Fitzpatrick (1999) extinction law. The internal extinction clearly depends on the internal properties of the observed source. Starburst objects are usually dusty and, therefore, we expect to have high internal extinction. We note that the spectral coverage of our observations do not allow us to derive the Hα/Hβ ratio to determine the internal extinction through the Balmer decrement. Therefore, to correct for this effect, we used the spectra published by Mendes de Oliveira et al. (2006) to obtain an average nebular colour excess for the central region of HCG 31A+C. In this case, the nebular colour excess was estimated using the observed Hα/Hβ ratio and comparing it with the expected value listed in Osterbrock (1989), using the recipes given in Domínguez et al. (2013). We obtain an average nebular colour excess of $E(B - V) \sim 0.08$ mag. Given that HCG 31A and HCG 31C are starburst objects (Gallagher et al. 2010), we used the Calzetti et al. (2000) extinction law to correct our data for internal extinction, considering the nebular colour excess estimated above (which is a factor of ~ 2 larger than the stellar colour excess). Note that the extinction correction is not a critical issue for line ratios (given that the emission lines display a small wavelength separation). However, this correction is important for the estimation of Hα luminosities and star formation rates (SFRs).

3.2 Flux measurements

The main nebular emission lines available in our data correspond to [N II] $\lambda 6548$ Å, Hα $\lambda 6563$ Å, [N II] $\lambda 6584$ Å, [S II] $\lambda 6717$ Å and [S II] $\lambda 6731$ Å. The available spectral resolution of FWHM = 2.4 Å

[~ 114 km s^{-1}, a value adopted from method (ii), see the next section] does not allow us to resolve multiple components in each emission line profile. For this reason, fluxes were estimated by fitting a single Gaussian on each observed line, using FLUXER,[3] which allows us confidently to determine the continuum level around the emission lines. The stellar continuum definition was made in the wavelength range 6620–6690 Å. The output parameters of this procedure are flux, continuum, width, centre, equivalent width and uncertainties derived from the 2D maps. Fluxes were compared with the values estimated by fitting a single Gaussian with the MPFIT code[4] and with the task SPLOT in IRAF, and the results are fully consistent. Given that, we have included the Hα emission and stellar continuum emission maps in the top and bottom panels of Fig. 4, respectively.

3.3 Velocity measurements

The most intense emission line in our data set is Hα. This emission line is usually used to analyse the kinematics of the warm gas in galaxies (e.g., Amram et al. 2007). We used it to derive the velocity field of the central region of HCG 31. As described above, the Gaussian fitting gives us the centre of each emission line. In this case, the estimated centre was converted into velocity, yielding a velocity field. In a similar way, we used the width of the profiles to produce a velocity dispersion map. At first order, if we suppose that the different emission line profiles can be fitted by Gaussians, the velocity dispersion σ corrected for instrumental and thermal broadening could be written as: $\sigma = \sqrt{\sigma_{obs}^2 - \sigma_{inst}^2 - \sigma_{th}^2}$, where σ_{obs} is the measured velocity dispersion for the observed profile. The instrumental width σ_{inst} was estimated in two different

---

[3] Interactive routine in IDL written by Christof Iserlohe. http://www.ciserlohe.de/fluxer/fluxer.html

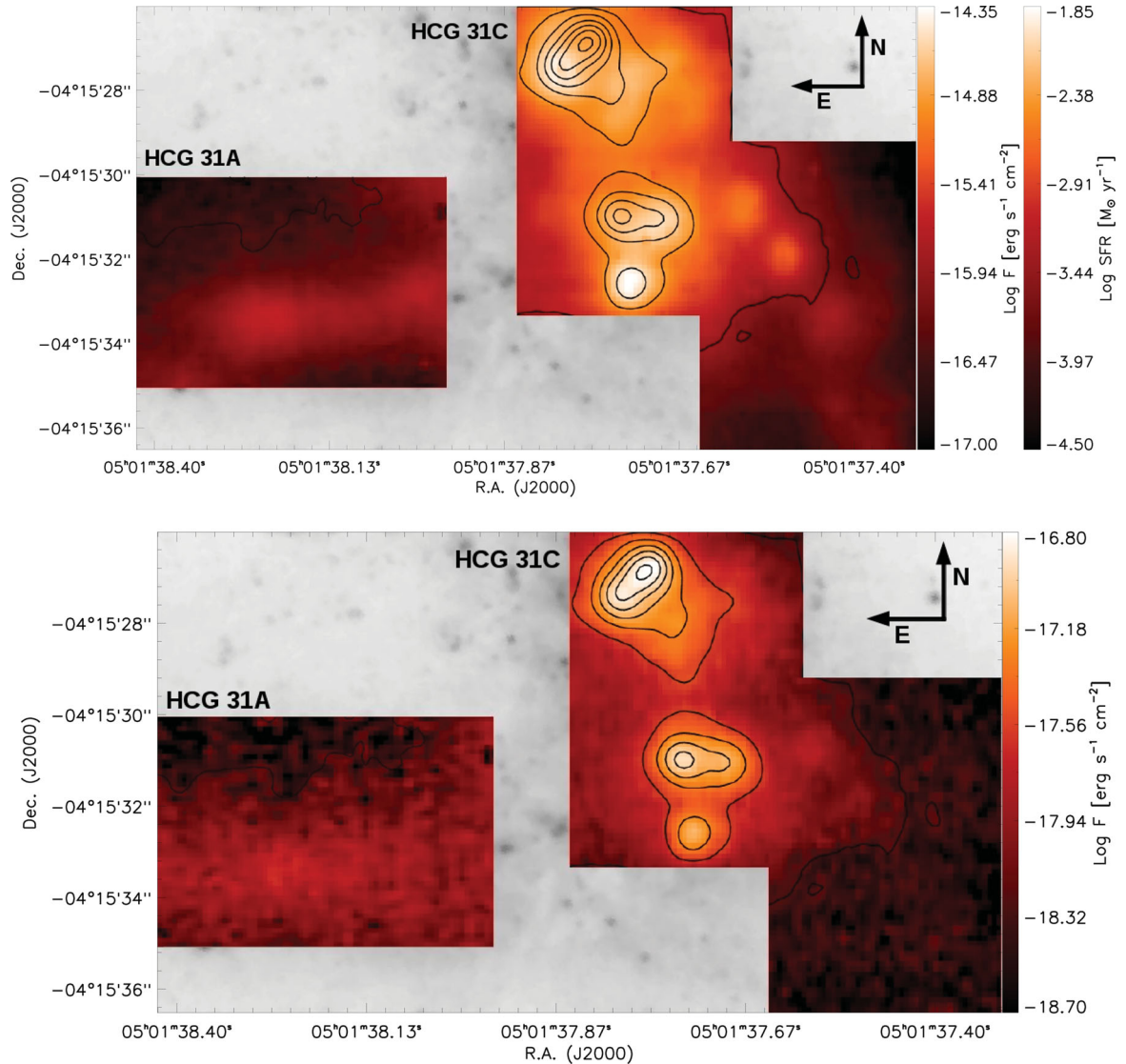[4] Fitting program package in IDL written by Craig B. Markwardt, NASA/GSFC Code 662, Greenbelt, MD 20770.

Figure 4. Top panel: Hα map for the central region of HCG 31A+C. In the same figure we have included a colour bar indicating the estimated SFRs. Bottom panel: Stellar continuum emission for the central region of HCG 31A+C. Both emission maps are in units of erg s⁻² cm⁻² and the black contours represent the stellar continuum emission.

ways, which resulted in consistent values: (i) from the average of the FWHM of the lines from the CuAr calibration lamp close to Hα, obtaining a spectral resolution of ~2.3 ± 0.1 Å, corresponding to ~110 km s⁻¹, leading to a resolution $R \sim 2850 \pm 125$ (in Hα), and (ii) following the method published by Sánchez et al. (2012), who estimate the spectral resolution by fitting a Gaussian in the most intense sky lines in one frame. In our case, we obtained an average of ~2.4 ± 0.1 Å, corresponding to ~114 km s⁻¹, leading to a resolution $R \sim 2730 \pm 115$. Finally, we adopt the value obtained from the second method. From this method, we estimated an instrumental width of $\sigma_{\rm inst} \sim 46 \pm 10$ km s⁻¹, where the uncertainty is represented by the standard deviation following Sánchez et al.'s (2012) method. We found a change in the value of the instrumental width across each observed field. On average, this variation is of the order of ~10 km s⁻¹. However, we note that the largest changes in this parameter occur at the edge of the fields, while in the centre of the fields the variation in the instrumental width is close to ~6 km s⁻¹. For the thermal width correction, we assumed $\sigma_{\rm th} = 9$ km s⁻¹, which corresponds to an electron temperature of 10 000 K (which is consistent

with the temperatures estimated by López-Sánchez et al. 2004). The uncertainty associated with the corrected velocity dispersion was estimated by propagating in quadrature the uncertainties of $\sigma_{\rm inst}$ and $\sigma_{\rm obs}$. The top and bottom panels of Fig. 5 are the velocity and velocity dispersion maps, respectively.

3.4 Star formation rates

There are several tracers of star formation. For example, the ultraviolet (UV) radiation emerging from young hot stars can be used to estimate the SFR of galaxies. However, this emission considers stellar populations with ages up to ~200 Myr. Also, this emission is strongly affected by dust attenuation. To mitigate these problems, several authors use UV and IR emission (e.g., Iglesias-Páramo et al. 2006, and more recently Eufrasio et al. 2014), to take into account the emission of dust that is heated by the strong UV radiation field. Another way to estimate SFRs is to use the Hα emission, which emerges from gas ionized by massive stars. Given the available data, the SFRs in HCG 31A+C have been
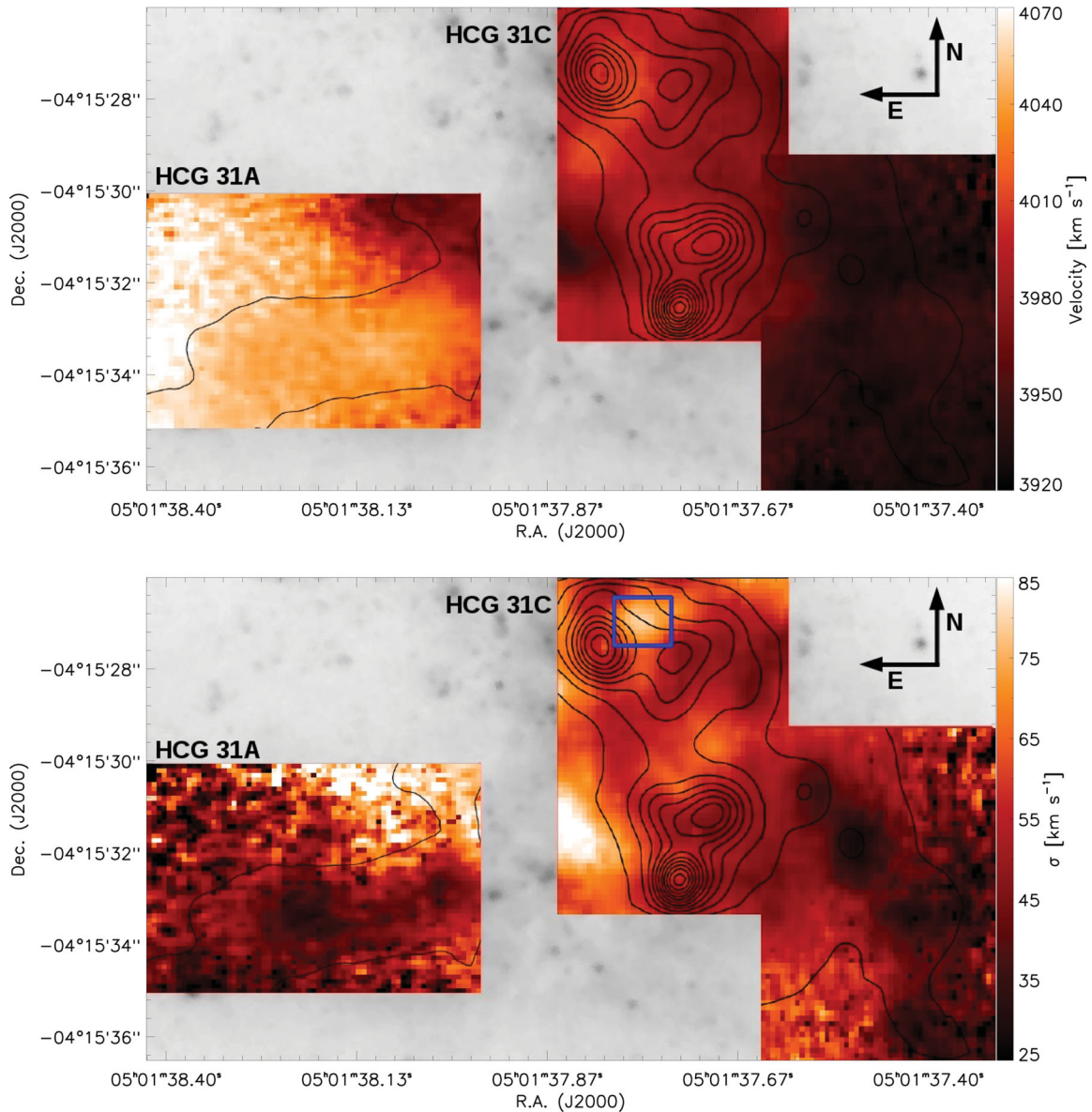
Figure 5. Top panel: Velocity map of the central region of HCG 31A+C. Bottom panel: Velocity dispersion map of the central region of HCG 31A+C. The overplotted blue box is the feature with high velocity dispersion values ($\sim$70–85 km s^{-1}). Black contours overplotted on the maps represent the Hα emission.

estimated using its Hα luminosity and the recipe given in Kennicutt (1998), which assumes a continuous star formation process, giving SFR$_{H\alpha}$ = 7.94 $\times$ 10^{-42} $\times$ L(Hα). However, we note that SFRs derived from Hα emission can be underestimated given that this emission is affected by extinction, which corresponds to one of the most important sources of uncertainty in the determination of SFR when using Hα luminosities (Kennicutt 1998). In the current analysis, we derived an average extinction for the region under study, which comes from the Balmer decrement of archival long-slit observations. Of course, the extinction can vary along the extension of HCG 31A+C, given the strong burst of star formation located in this region. Therefore, we caution the reader that our estimations of SFRs may be affected by spatial variation in the extinction, therefore, our SFRs may be overestimated (which is discussed in Section 5.1).

3.5 Electron densities

Our spectroscopic data cover the [S II] lines, [S II] λ6717 Å and [S II] λ6731 Å. We calculated the electron density (N_e) from the observed [S II] λ6717 Å/[S II] λ6731 Å ratio using the task TEMDEN, which belongs to the IRAF STSDAS NEBULAR package. The task TEMDEN implements the five-level atomic model FIVEL (De Robertis, Dufour & Hunt 1987). We were not able to estimate the electron temperatures due to the spectral coverage ($\sim$5620–6980 Å). So, in this case we assumed an electronic temperature of $T_e = 10\,000$ K. This assumption is consistent with the electronic temperature found by López-Sánchez et al. (2004) for the burst associated with HCG 31C ($T_e = 10\,800 \pm 300$ K, table 3 in that paper). The uncertainties in the estimates are represented by the standard deviation. The electron density map obtained using this method is shown on the top panel of Fig. 6.
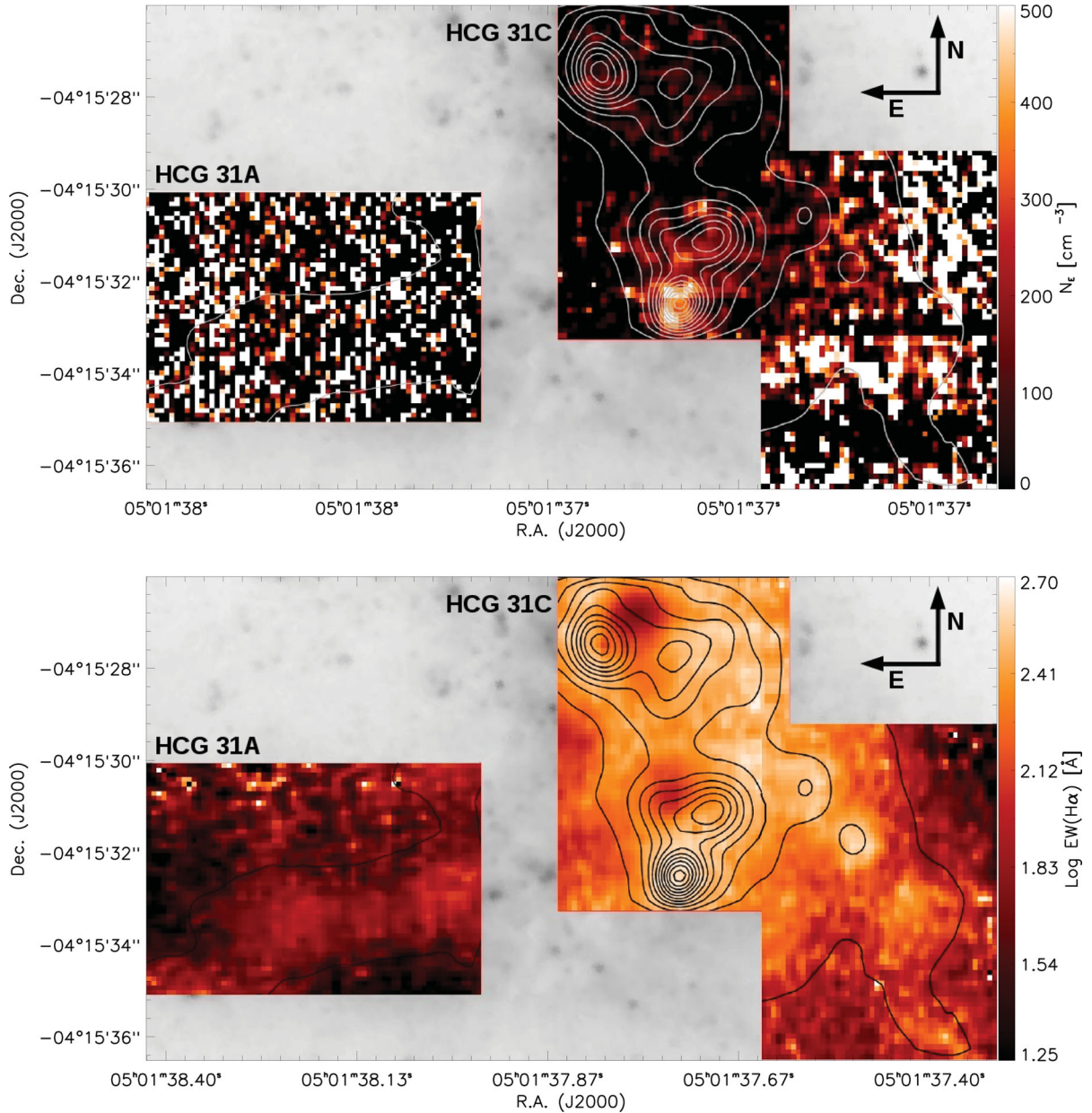
Figure 6. Top panel: Electron density map for the central region of HCG 31A+C. Bottom panel: Hα equivalent width map for the central region of HCG 31A+C. Black and white contours overplotted on the maps represent the Hα emission.

3.6 Hα equivalent width and age determination

We estimated the ages of the bursts by comparing the measured Hα equivalent width [EW(Hα)] with Starburst99 modelled values (Leitherer et al. 1999). Considering that the oxygen abundances in the regions of interest range from $12 + \log(O/H) \sim 8.2$ to ~ 8.5 (López-Sánchez et al. 2004; Torres-Flores et al. 2015), the Starburst99 models were generated for a single stellar population with metallicities of $Z = 0.004$ and $Z = 0.008$,[5] which correspond to $Z = 0.2$–$0.4\ Z_\odot$, and Salpeter initial mass function (IMF) with masses ranging between 1 and 100 $M_\odot$. The map obtained for the

estimated values of EW(Hα) is shown in the bottom panel of Fig. 6 and the age maps are shown in the top and bottom panels of Fig. 7.

4 RESULTS

In Figs 4, 5, 6 and 7, we show different maps that we derived from the IFU observations of HCG 31A+C. In Tables 1 and 2 are shown the luminosities and SFRs, and the main physical properties estimated for this system, respectively.

4.1 Hα emission and star formation rates

In the top panel of Fig. 4, we show the Hα emission flux map of the central region of HCG 31A+C. In the figure, the black contours represent the stellar continuum emission, which was derived from
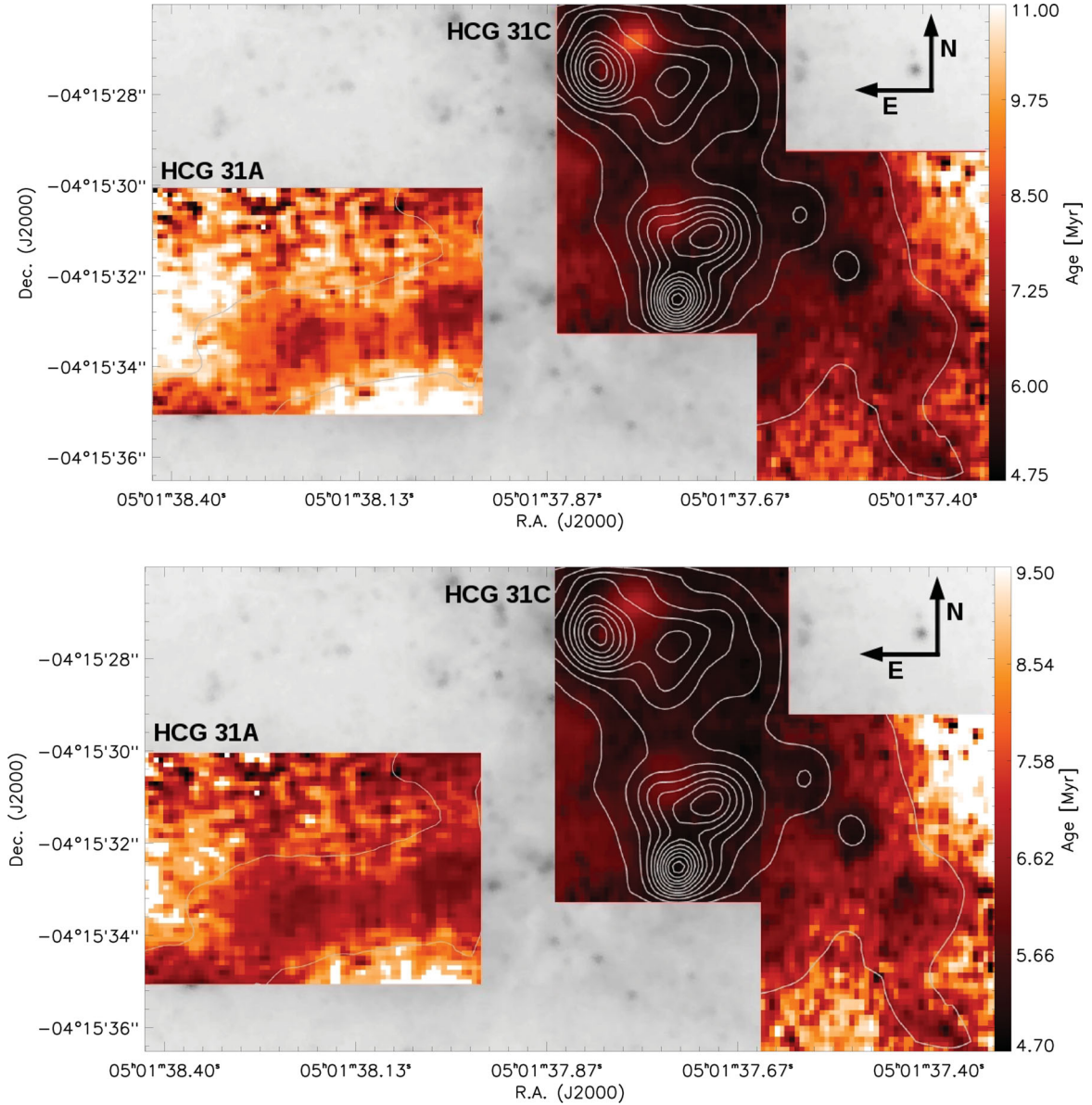
---

[5] We used the conversion $Z = Z_\odot \times 10^{(\log(O/H) - 12 + 3.1)}$ and assumed $\log(O/H)_\odot = -3.10$ (Fiorentino et al. 2012), and a solar metallicity of $Z_\odot = 0.018$ (Allende-Prieto, Lambert & Asplund 2001).

Figure 7. Top panel: Age map estimated assuming an instantaneous star formation law for the central region of HCG 31A+C for a metallicity of $Z = 0.004$. Bottom panel: Like the top panel, but for $Z = 0.008$. Both cases are for a Salpeter IMF with a mass limit of 1–100 M$_\odot$. In both panels, white contours overplotted on the map represent the Hα emission.

Table 1. Luminosities and SFRs of HCG 31A+C.

Source	$L_{H\alpha}^{b,d}$ $\times 10^{41}$ erg s^{-1}	$L_{H\alpha}^{b,e}$ $\times 10^{41}$ erg s^{-1}	$L_{H\alpha}^{b,f}$ $\times 10^{41}$ erg s^{-1}	SFR^{c,d} M$_\odot$ yr^{-1}	SFR^{c,e} M$_\odot$ yr^{-1}	SFR^{c,f} M$_\odot$ yr^{-1}
Burst HCG 31C[a]	1.43 ± 0.13	1.55 ± 0.14	1.89 ± 0.18	1.13 ± 0.11	1.22 ± 0.11	1.49 ± 0.14
Burst HCG 31A[a]	1.31 ± 0.12	1.42 ± 0.13	1.73 ± 0.16	1.03 ± 0.10	1.12 ± 0.10	1.37 ± 0.13
HCG 31 east	0.63 ± 0.06	0.70 ± 0.65	0.87 ± 0.08	0.50 ± 0.05	0.55 ± 0.05	0.69 ± 0.06
HCG 31 centre	8.77 ± 0.82	9.50 ± 0.89	11.60 ± 1.08	6.93 ± 0.65	7.51 ± 0.70	9.16 ± 0.85
HCG 31 west	1.16 ± 0.11	1.26 ± 0.17	1.53 ± 0.14	0.92 ± 0.09	0.99 ± 0.09	1.21 ± 0.11
HCG 31 all	10.56 ± 0.83	11.46 ± 1.12	14.00 ± 1.10	8.35 ± 0.66	9.05 ± 0.71	11.06 ± 0.86

Notes. [a]Considering a box of 1.1×1.1 arcsec, corresponding to 298×298 pc. [b]Estimated using the integrated Hα emission flux. [c]Using the measured integrated $L_{H\alpha}$ luminosity as input to Kennicutt's (1998) formula (2), and assuming continuous star formation. [d]Value before extinction correction. [e]Value corrected by Galactic extinction using the Fitzpatrick extinction law. [f]Value corrected by Galactic extinction using the Fitzpatrick extinction law, and internal extinction using the Calzetti extinction law with a nebular colour excess of $E(B - V)_{gas} = 0.08$ mag.

Table 2. Main physical properties of bursts in HCG 31A+C.

Source	$12 + \log(\text{O/H})^c$	$N_e^{b,d}$ cm^{-3}	EW(Hα)^{b,e} Å	Age^{b,f} Myr	Age^{b,g} Myr
Burst in HCG 31C^a	8.22 ± 0.17	82 ± 50	238 ± 90	6 ± 2	5 ± 2
Burst in HCG 31A^a	8.44 ± 0.16	228 ± 120	338 ± 50	5 ± 1	5 ± 1

Notes. ^{a}Considering a box of 1.1 × 1.1 arcsec, corresponding to 298 × 298 pc. ^{b}Mean value, where the associated uncertainties correspond to the standard deviation. ^{c}Estimated by Torres-Flores et al. (2015) using the N2 calibrator published by Marino et al. (2013).^{d}Estimated using the task TEMDEN in the IRAF STSDAS NEBULAR package. ^{e}Obtained with using the IDL routine FLUXER written by Christof Iserlohe. ^{f}Using the measured EW(Hα) as input to the Starburst99 code, assuming instantaneous star formation with a metallicity of $Z = 0.004$ and a Salpeter IMF (Leitherer et al. 1999). ^{g}Using the measured EW(Hα) as input to the Starburst99 code, assuming instantaneous star formation with a metallicity of $Z = 0.008$ and a Salpeter IMF (Leitherer et al. 1999).

the IFU data, and we trace the stellar emission in this region (see bottom panel of Fig. 4). Inspecting this figure, we detect four strong Hα sources. The northern objects are linked with the galaxy HCG 31C, while the southern sources belong to the member HCG 31A. We also detect diffuse Hα emission across the three observed fields.

The bottom panel of Fig. 4 shows the stellar continuum map. For HCG 31C, there is an offset between the peak of the continuum and the Hα emission. The continuum peaks 1 arcsec (~270 pc) to the north-west of the maximum in the Hα emission. This feature has not been previously identified in the central region of HCG 31A+C. This can bring some new insights regarding the star formation processes in this merging system. A possible scenario for this phenomenon is discussed in the next sections. In general, our Hα map is in agreement with the Hα image published by Vilchez & Iglesias-Páramo (1998). Using our data set, we derived the Hα luminosities of the two main bursts associated with HCG 31C and HCG 31A, which display luminosities of $L_{\text{H}\alpha} = 1.89 \times 10^{41}$ erg s^{-1} and $L_{\text{H}\alpha} = 1.73 \times 10^{41}$ erg s^{-1}, respectively. Clearly these values exceed the luminosity of the well-known giant H II regions (like 30 Doradus, which has a luminosity of $L_{\text{H}\alpha} \sim 3 \times 10^{39}$ erg s^{-1}, López et al. 2014). The bursts detected in HCG 31A and HCG 31C have been studied in the past by Johnson & Conti (2000), who found that the galaxy component AC shows signs of star formation over the past ~10 Myr, and a peak in the EW(Hα) distribution corresponding to star formation about ~5 Myr ago. For the star-forming complexes associated with HCG 31C, López-Sánchez et al. (2004) detected Wolf–Rayet features, which is consistent with a young stellar population. These authors also suggest an age of 5 Myr for the complex associated with HCG 31C, and an age of 7 Myr for member HCG 31A. However, the current analysis allows us to study in detail the physical properties of these bursts, given that we have spectroscopic information for each spaxel.

Following Kennicutt (1998), the above Hα luminosities were used to estimate the SFRs in the central region of HCG 31A+C. The right colour bar in the top panel of Fig. 4 indicates the logarithmic SFRs in the HCG 31A+C complex. The figure shows a peak in the SFR located in the HCG 31A complex, which seems to be more compact than the region located to the north. We estimate SFR = 1.49 M$_\odot$ yr^{-1} and SFR = 1.37 M$_\odot$ yr^{-1} for the northern and southern star-forming regions, HCG 31C and HCG 31A, respectively. Then, for the whole complex, we estimate SFR ~2.86 M$_\odot$ yr^{-1}, which is consistent with the value derived by López-Sánchez et al. (2004) for the region HCG 31A+C (see their table 9). When we derived the SFR for each observed field (east, centre and west), we found that fields east and west display a modest SFR, compared with the SFR derived for the central field (0.69, 9.16 and 1.21 M$_\odot$ yr^{-1}, respectively). All these values are listed in Table 1, including the uncertainties associated with these mea-

surements. Integrating the SFR for all the observed members of HCG 31A+C, we determine SFR = 11.06 M$_\odot$ yr^{-1}. Gallagher et al. (2010) used UV and IR information to derive the SFR of all members of HCG 31, finding a value of ~10.6 M$_\odot$ yr^{-1}. They note that the main contribution to the SFR comes from members A+C and E. Some possible reasons for the discrepancies between both determinations are mentioned in Section 5.1.

4.2 Kinematics: Velocity fields and velocity dispersion maps

In the top panel of Fig. 5, we show the velocity field of the central region of HCG 31. The uncertainty associated with the radial velocities is ~10 km s^{-1}, which was estimated by adding in quadrature the error in the wavelength calibration and the FWHM. We found that the main star-forming bursts in HCG 31A and HCG 31C display similar radial velocities, which reach values of ~4000 km s^{-1}. Although we have a small field of view in our observations, we observe a perturbed velocity field. We cannot identify a kinematic major axis. This suggests that non-circular motions are present in the central region of HCG 31, which is expected, given the strong signatures of interactions. In general, the velocity field presented in Fig. 5 is in agreement with the kinematic analysis presented by Amram et al. (2007).

The velocity dispersion map for HCG 31A+C is presented in the bottom panel of Fig. 5. The uncertainty associated with the velocity dispersion is 13 km s^{-1}. The two main bursts of star formation, belonging to HCG 31A and HCG 31C, display velocity dispersions of ~55 km s^{-1}. In this figure, the most interesting feature corresponds to a region located in HCG 31C, which displays quite high velocity dispersions of ~85 km s^{-1}. It is identified by a blue box. The velocity dispersion in this region differs by at least 1σ (13 km s^{-1}) from that of its neighbourhood, as calculated by considering the largest variation across the field, in an area of 5 × 7 arcsec (~10 km s^{-1}). The variation across an area of 2 × 5 arcsec, in the central region where the feature is located, is smaller (~6 km s^{-1}). Considering this, we suggest there is a peak in the velocity dispersion located in this area. This source lies at the same spatial position as the peak in the continuum contours (see bottom panel of Fig. 4). Given the medium spectral resolution of our observations, this broadening may emerge as the sum of, at least, two components of the Hα emission line. These components may be associated with ionized gas that is being blown out by a star cluster, which can be identified with the continuum information. We speculate that the offset between the Hα and continuum emission at this location (the star-forming burst in HCG 31C) is produced by a stellar cluster, which is cleaning its environment. This process may be triggering star formation in its neighbourhood, and that is why we observe a strong Hα-emitting source close to the continuum peak. This kind

of phenomenon has been studied in local giant star-forming regions, such as N11 (Walborn & Parker 1992; Barbá et al. 2003) and in the H II region NGC 604 in M33 (Maíz-Apellániz, Pérez & Mas-Hesse 2004; Tosaki et al. 2007; Barbá et al. 2009; Fariña, Bosch & Barbá 2012; Martínez-Galarza et al. 2012).

4.3 Oxygen abundances and electron densities

The oxygen abundance map of the central region of HCG 31A+C has been recently published by our group (Torres-Flores et al. 2015). This map was derived using the N2 index, which is defined as:

$$N2 = \log([N\,\textsc{ii}]\lambda 6584/H\alpha), \tag{1}$$

and using the Marino et al. (2013) calibration. Torres-Flores et al. (2015) found a smooth metallicity gradient between HCG 31A and HCG 31C (1.5×10^{-4} dex pc^{-1}). Inspecting high-resolution Fabry–Perot data published by Amram et al. (2007), they found a gas flow between the two galaxies, which confirms the scenario of metal mixing produced by gas flows, given the smooth gradient between HCG 31A and HCG 31C.

In the top panel of Fig. 6, we show the electron density map of HCG 31A+C, where the contours represent the Hα emission. Given the low intensity of the [S II] $\lambda\lambda 6717, 6731$ Å emission lines, most of the information comes from the main star-forming burst. The burst associated with HCG 31A displays an average electron density of $N_e = 228 \pm 120$ cm^{-3}, with a peak of $N_e \sim 500$ cm^{-3}. For the galaxy HCG 31C, the average is $N_e = 82 \pm 50$ cm^{-3}, reaching a peak of $N_e \sim 150$ cm^{-3}. López-Sánchez et al. (2004) estimated the electron density for the different components of HCG 31. For HCG 31C, these authors found a value of $N_e = 270 \pm 70$ cm^{-3} (the value for HCG 31A was not estimated). However, we note that our data allow us to obtain the electron density for each spaxel in HCG 31A+C. Therefore, this can affect any comparison with previous results, which mainly have been obtained from long-slit spectroscopy.

4.4 Hα equivalent width and age estimation

Given that the Hα emission traces recent star formation, EW(Hα) can be used to estimate the ages of these events (e.g., Leitherer & Heckman 1995). The Hα equivalent width is important since it gives us an estimation of the ratio between the ionizing photons from massive stars and the continuum photons from the stellar population and gas (Cedrés, Cepa & Tomita 2005). The bottom panel of Fig. 6 shows EW(Hα) values for the central region of HCG 31A+C, where the contours represent the Hα emission. EW(Hα) varies over $18 < \text{EW}(H\alpha) < 501$ Å. For the two main bursts, we estimated a mean value of EW(Hα) =338 ± 50 Å for the burst in HCG 31A and EW(Hα) =238 ± 90 Å for the burst in HCG 31C, which are similar to those measured for the star-forming complexes in the west region.

From the EW(Hα) values, we estimated the age of the star-forming objects located in the central region of the system HCG 31A+C. These maps are shown in Fig. 7. In the top and bottom panels, the ages were estimated by assuming a metallicity of $Z = 0.004$ and $Z = 0.008$, respectively. In both maps, the contours represent the Hα emission. Inspecting the top panel ($Z = 0.004$), we can observe ages ranging from 5 to 11 (± 2) Myr, through the east, centre and west regions. In the bursts associated with the galaxies HCG 31C and HCG 31A, we have estimated a mean age of 6 ± 2 and 5 ± 1 Myr, respectively. Considering the uncertainties, we suggest that both bursts have similar ages. The bottom panel in Fig. 7
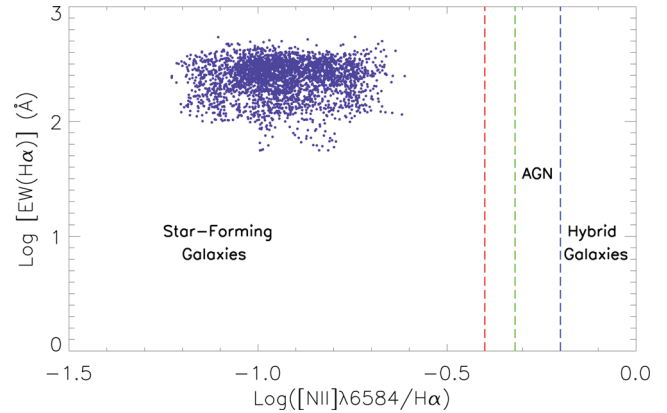

Figure 8. Diagnostic diagram of EW(Hα) versus N2. Values are for the centre region. The limits proposed by Stasińska et al. (2006) for galaxy classification are: red dashed line for star-forming galaxies with $-0.4 < \log([N\,\textsc{ii}]/H\alpha)$; the region between the red and blue dashed lines corresponds to AGNs with $-0.4 < \log([N\,\textsc{ii}]/H\alpha) < -0.2$; and the blue dashed line shows the limit for hybrid galaxies with $\log([N\,\textsc{ii}]/H\alpha) > -0.2$. The green dashed line is the limit proposed by Kauffmann et al. (2003) to distinguish between star-forming galaxies and AGNs, corresponding to $-0.32 < \log([N\,\textsc{ii}]/H\alpha)$.

($Z = 0.008$) shows similar ages with small variations, but following the same trend with ages of 5–10 (± 2) Myr.

We also estimated the age at the same location of the stellar continuum emission peak (see bottom panel of Fig. 4) and we obtain an age of 9 Myr, while the Hα emission peaks in the burst associated with HCG 31C have an age of 5 Myr (see top panel of Fig. 4). This result is in agreement with the scenario we proposed in Section 4.2, where the stellar continuum emission is from a stellar cluster (~ 9 Myr), which would clean the interstellar medium (ISM) and trigger star formation around it (~ 5 Myr). The lowest ages are found in the galaxy HCG 31C and (even considering the uncertainties) are consistent with Wolf–Rayet stars. This is consistent with the spectrum of this region published by López-Sánchez et al. (2004).

Although previous works have already dated some star-forming regions in HCG 31, the IFU data allow us to estimate the ages of different structures in a spatially resolved way, like in the star-forming regions in HCG 31A and HCG 31C, and the east, centre and west regions. Also, the current results show that the region where the super stellar cluster candidate lies is older than the burst associated with the galaxy HCG 31C. This allows us to add a new piece of evidence to the scenario we proposed of a stellar cluster cleaning its environment and triggering star formation. On the other hand, other authors have estimated the ages for a more global area in this system (e.g., López-Sánchez et al. 2004; Johnson & Conti 2000), which range from 5 to 10 Myr.

4.5 Ionizing mechanism

To analyse the ionizing mechanism in the centre region of HCG 31A+C (where most of the Hα emission arises), we have included an EW(Hα) versus N2 [log([N II]/Hα)] diagnostic diagram, which is presented in Fig. 8. This kind of diagram was proposed for the first time by Cid Fernandes et al. (2010), who used the gas ionization mechanism to classify their galaxy sample, with limits proposed by Kewley et al. (2001), Kauffmann et al. (2003) and Stasińska et al. (2006). Cid Fernandes et al. (2010) point out the utility of these diagrams, which arises from the information we can get from
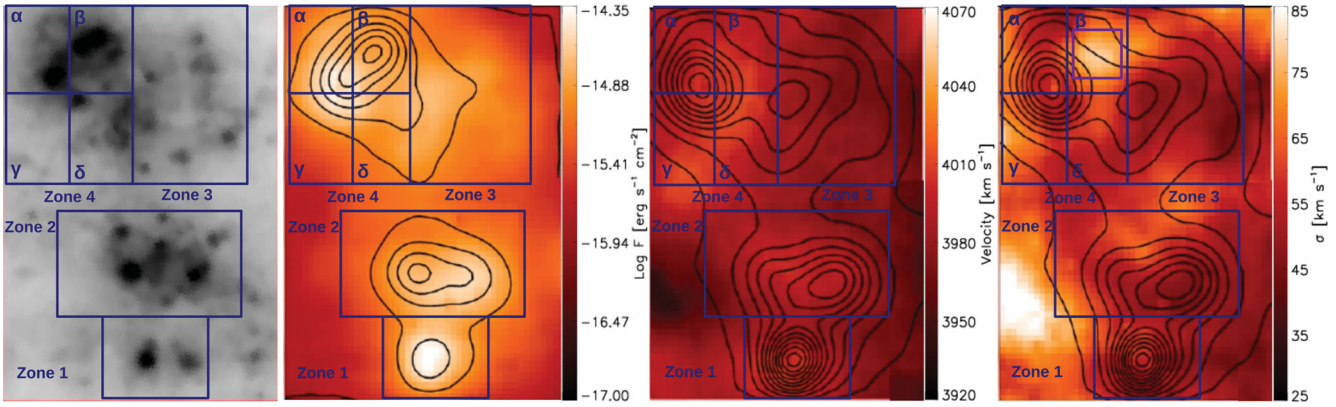
Figure 9. From left to right, the centre region from (1) the optical HST image (from Fig. 3), (2) the Hα flux map whose contours are the stellar continuum emission (from Fig. 4), (3) the velocity field map and (4) the velocity dispersion map (both from Fig. 5). The blue squares show the four zones with the highest Hα emission in the centre region, denominated as zones 1, 2, 3 and 4. Zone 4 is subdivided into sub-zones α, β, γ and δ. The purple square overplotted in the last panel is located at the position of the suggested *shell* in this region, with an area of 0.58×0.58 arcsec (158×158 pc).

both physical parameters (EW and N2). First, they mention that the line ratio can give information of the physical conditions of the ionized gas, and EW(Hα) provides an estimation of the ionization power of the stellar population. Kauffmann et al. (2003) present a classification based on the [N II]/Hα ratio, proposing an upper limit of $-0.32 < \log([N\,\text{II}]/H\alpha)$ for star-forming galaxies (green dashed line in Fig. 8). Stasińska et al. (2006) present techniques to distinguish star-forming galaxies from galaxies with an active galactic nucleus (AGN). One of these is also based on the [N II]/Hα ratio, where $-0.4 < \log([N\,\text{II}]/H\alpha)$ is for star-forming galaxies (red dashed line in Fig. 8); $-0.4 < \log([N\,\text{II}]/H\alpha) < -0.2$ is for AGNs (the region between the red and blue dashed lines in Fig. 8); and $\log([N\,\text{II}]/H\alpha) > -0.2$ is for hybrid galaxies (blue dashed line in Fig. 8). In these diagrams, the limits proposed for the galaxy classification given by Kauffmann et al. (2003) and Stasińska et al. (2006) are approximately vertical. This allows us to carry out this classification considering the [N II]/Hα ratio (Cid Fernandes et al. 2010).

In Fig. 8, we note that the N2 values for HCG 31A+C are in the range $-1.2 < \log([N\,\text{II}]/H\alpha) < -0.5$ (purple points), while the EW(Hα) values are in $1.3 < \log(\text{EW}(H\alpha)) < 2.7$. In this diagram, we can observe that the centre region is placed over a region where the gas in the galaxies is ionized by star formation according to the limits proposed by Kauffmann et al. (2003) (green dashed line) and Stasińska et al. (2006) (red dashed line). From these results we conclude that the ionizing mechanism in HCG 31A+C is star formation, and we can exclude AGN activity.

4.6 Intensity versus σ plots

In Section 4.2, we suggest that there is a super stellar cluster in HCG 31C, which is cleaning its environment and triggering star formation in its vicinity. This suggestion is supported by the measured velocity dispersion at that location. This kind of phenomenon has been reported for other systems, but for the first time, we suggest these events are taking place in the main central region of HCG 31A+C, in the interface area between the galaxies HCG 31A and HCG 31C. To investigate the presence of this structure (or maybe also other structures) and the plausibility of a possible wind-triggered star-forming scenario, we divided the centre region into four zones (by considering the major Hα emission regions) and we present σ versus flux diagrams for these zones. These are represented by blue

squares in the four panels of Fig. 9, which are enumerated as zones 1, 2, 3 and 4. In this figure, from left to right, the panels correspond to the centre region extracted from (1) the optical HST image (Fig. 3), (2) the Hα emission map (Fig. 4) with the stellar continuum emission represented by the black contours, (3) the velocity field map (Fig. 5) and (4) the velocity dispersion map (Fig. 5) where the contours represent the Hα emission. In the last panel of Fig. 9, we have overplotted a purple square, which represents the super shell produced by the suggested super stellar cluster in this region, which has an area of 0.58×0.58 arcsec (158×158 pc).

The σ versus flux diagnostic diagrams are a useful tool for identifying the mechanism that broadens the emission line profile (i.e., Muñoz-Tuñón et al. 1996; Martínez-Delgado et al. 2007; Moiseev & Lozinskaya 2012). In the top panel in Fig. 10, we present the sigma versus flux diagram for the four zones in the centre region, while the middle and bottom panels are the radial velocity versus flux and σ versus radial velocity diagrams, respectively. In the three diagrams, the blue, green, black and red symbols correspond to zones 1, 2, 3 and 4, respectively. Grey symbols represent the points that do not belong to any of these zones. Analysing the σ versus flux diagram, we can see that zone 4 (red symbols) shows a different spatial distribution in comparison with the other regions, with the highest velocity dispersions of the centre region ($\sigma \sim 60$–$85 \, \text{km s}^{-1}$) and fluxes up to $\sim 3.7 \times 10^{-15} \, \text{erg s}^{-1} \, \text{cm}^{-2}$.

This difference is also observed in the radial velocity versus flux (middle panel) and σ versus radial velocity (bottom panel) diagrams. This zone displays a wide velocity range of 3985–$4015 \, \text{km s}^{-1}$, with a predominance of high velocity values. This could indicate the existence of several structures in the centre region, where each structure has different kinematic behaviour. This could suggest that the broadening mechanism for the Hα line profile in zone 4 is different to that in the other zones. On the other hand, from the position of the grey symbols in the σ versus flux diagram (top panel of Fig. 10), we can say these do not belong to any knot or do not form a shell. They are part of the envelope that surrounds the H II regions.

4.6.1 Inspecting zone 4

Considering the distinctive behaviour of zone 4 in the three different diagnostic diagrams with respect to the other zones (which suggests they have a different and more complicated broadening mechanism),
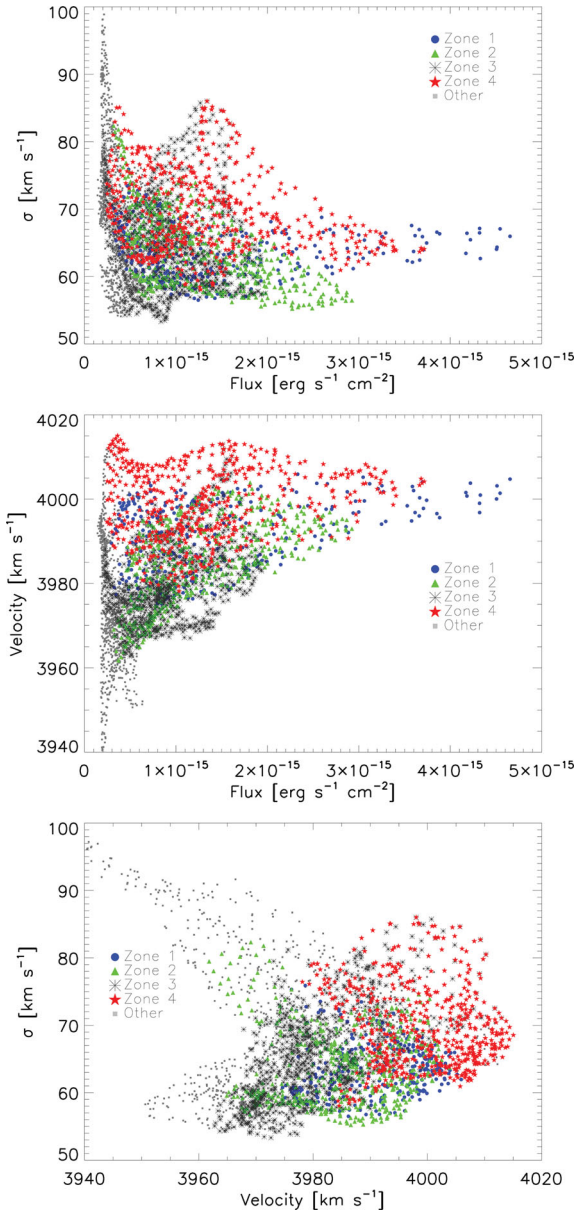
Figure 10. Top panel: σ versus flux diagram. Middle panel: Radial velocity versus flux diagram. Bottom panel: σ versus radial velocity diagram. Zones 1, 2, 3 and 4 are represented by blue, green, black and red symbols, respectively. Grey symbols represent the points that do not belong to any of these zones.

we subdivided it into four sub-zones called α, β, γ and δ (see Fig. 9) to analyse in more detail the phenomena in this zone. This division was made in an attempt to determine more accurately the number of structures present; while we expect at least two, there may be more.

We have included these three diagnostic diagrams for the four sub-zones in the left column of Fig. 11, where sub-zones α, β, γ and δ are represented by blue circles, green triangles, black asterisks and red stars, respectively. For clarity, the super shell in sub-zone β is highlighted with purple squares in the right-hand panels of Fig. 11 (corresponding to the purple square in the last panel in Fig. 9).

Analysing the σ versus flux diagram (top left panel of Fig. 11), we note two independent distributions, which are indicated with turquoise arrows. The right arrow indicates a structure in sub-zone

β (green triangles). This presents the highest velocity dispersion values, reaching 85 km s^{-1}. On the other hand, the left arrow shows a structure that seems to be composed by the other three sub-zones of zone 4. This last structure presents velocity dispersions in a range of ~55–80 km s^{-1}. This does not include the black asterisks of sub-zone γ, which present values of 80–85 km s^{-1}, because these points do not belong to the burst associated with the galaxy HCG 31C (see fourth panel in Fig. 9). In the second panel in Fig. 9, we note that sub-zone β presents the highest stellar continuum emission (black contours) and lowest Hα emission with respect to the other sub-zones, especially α, where most of the burst is located. This suggests that in sub-zone β there is an older stellar population than that observed in the other sub-zones, especially in the Hα burst. This offset between the peak in the Hα and stellar continuum emission may be linked with star formation triggered by the feedback of the super star cluster. Sub-zone α has the most intense Hα emission, of up to ~5×10^{-15} erg s^{-1} cm^{-2}, and with σ values lower than 80 km s^{-1}. Therefore, we cannot discount that there is more than one stellar population in zone 4. In fact, we report the finding of at least two stellar populations: the oldest is located in sub-zone β, and the other is in the other sub-zones, mostly in sub-zone α, which would be triggered by the feedback of the stellar cluster.

4.6.2 Inspecting the candidate super shell

To locate the points that belong to the super shell produced by the super stellar cluster candidate in sub-zone β, we have highlighted a region represented by a purple square in the last panel of Fig. 9, which has been plotted independently in the three diagnostic diagrams described previously (right panels of Fig. 11) and is represented by purple squares. Inspecting the σ versus flux diagram in the top right panel in this figure, this structure appears as a region delimited by a velocity dispersion of ~73–86 km s^{-1} and fluxes of 1.0–3.3 $\times 10^{-15}$ erg s^{-1} cm^{-2}, resulting in the most intense peak in this figure. Considering the difference in the velocity dispersion values (at least $1\sigma \sim 13$ km s^{-1}) between the super shell and its neighbourhood, we suggest there is a peak in the velocity dispersion located where the super shell is located.

The results found in the σ versus flux diagram for the super shell are consistent with the model proposed by Muñoz-Tuñón et al. (1996). This model describes a shell where the maximum σ value and the minimum surface brightness are detected at its centre. As the distance to the centre increases, up to the internal edge of the shell, the surface brightness increases and σ decreases. This super shell would correspond to the region delimited as the possible super shell (purple squares). Analysing the flux versus radial velocity diagram in the middle right panel in Fig. 11, we can see a vertical pattern in the purple squares, which represents the super shell in sub-zone β. This pattern describes a wide range of radial velocities (3985–4010 km s^{-1}) in a small range of intensities (1.0–2.2 $\times 10^{-15}$ erg s^{-1} cm^{-2}), which may indicate a local expansion of gas. Finally, in the radial velocity versus σ diagram in the bottom right panel in Fig. 11, the distribution of the purple squares does not present a clear pattern. This could indicate that the expansion is isotropic, with no defined direction. This kind of diagram and analysis (and pattern) were also carried out by Bordalo, Plana & Telles (2009), who found similar results for specific areas in an H II region in the galaxy Zw 40.

The ages estimated for sub-zones α and β are consistent with the scenario proposed above. The estimates (see Section 4.4) give an age of ~9 ± 2 Myr for the super stellar cluster in sub-zone β

and $\sim 5 \pm 2$ Myr for the Hα emission peak in sub-zone α, with a difference in age of ~ 4 Myr.

5 DISCUSSION

5.1 The main physical properties of HCG 31A+C

HCG 31 has been studied by several authors, in different wavelengths, in recent years. Rubin et al. (1990), Williams, McMahon & van Gorkom (1991), Iglesias-Páramo & Vilchez (1997), Vilchez & Iglesias-Páramo (1998), Johnson & Conti (2000), Verdes-Monetengro et al. (2005), Richer et al. (2003), Amram et al. (2004, 2007), López-Sánchez et al. (2004), Mendes de Oliveira et al. (2006) and Gallagher et al. (2010) studied the different physical processes that are taking place in this object. Several of these results suggest that the central region of HCG 31A+C is dominated by young and strong bursts of star formation, which have ages lower than 7 Myr. Rubin et al. (1990) and López-Sánchez et al. (2004) reported the presence of Wolf–Rayet features in the spectra of this system, which is consistent with even younger ages. Also, Mendes de Oliveira et al. (2006) found that the galaxy HCG 31C follows the luminosity–metallicity relation (in the K band) defined by dwarf irregular galaxies.

In this work, we have estimated a luminosity in Hα for the centre region in HCG 31A+C of $\log(L_{H\alpha}) = 42.06 \pm 0.09$ erg s^{-1}. This value is higher than the estimate of Iglesias-Páramo & Vilchez (1997), who also studied the Hα emission in HCG 31, obtaining a luminosity in Hα of $\log(L_{H\alpha}) = 41.66$ erg s^{-1} for the system HCG 31A+C. To correct for internal extinction, these authors used a colour excess of $E(B-V) = 0.15$. López-Sánchez et al. (2004), using the data published by Iglesias-Páramo & Vilchez (1997), estimated an Hα luminosity for this system of $\log(L_{H\alpha}) = 41.78$ erg s^{-1}, and $\log(L_{H\alpha}) = 41.54$ erg s^{-1} from their own spectroscopic data. The differences among these values can arise from the colour excess and the extinction law used. In our case, we estimated an average value for the colour excess that was derived from the long-slit observations of the system HCG 31A+C. This correction was applied to the three observed fields of view. In this sense, our luminosities may be over- or underestimated, given the use of an average value for $E(B-V)$. Also, we need to keep in mind that the dust distribution in this system is not uniform. In fact, Gallagher et al. (2010) observed that the dust emission is higher in the interface zone between galaxies HCG 31A and HCG 31C. Therefore, considering we have used the slit that crosses this region for the colour excess estimate, this could overestimate the fluxes in the rest of the fields observed. However, the main part of this study is focused in the interface region, where the slit is located, therefore this could work at least in this context. Other facts to be considered for the different luminosity values are the flux calibration, which is not absolute and could result in an overestimation of the fluxes, the area over which we have integrated the luminosities and the observational technique (IFU versus long-slit versus Hα imaging).

The velocity field of HCG 31A+C is perturbed. Clearly, even if the grand pattern motion displays globally a rotation movement, it does not show the fingerprint of a simple disk in rotation, given the complex structure of the system. This is consistent with the map derived by Amram et al. (2007), which covers the entire compact group. On the other hand, the spatial resolution of the IFU observations allows us to distinguish structures in the central region of HCG 31A+C, which present different velocity dispersion values. This has allowed us to detect a structure with the highest σ values in the central region of HCG 31A+C, which is located in one of the

star-forming complexes (complex 1) detected by Gallagher et al. (2010, their fig. 4). These authors propose that these complexes could be formed by several stellar clusters, so complex 1 could include the star formation burst associated with the galaxy HCG 31C and a stellar cluster, which we suggest is cleaning its environment and triggering star formation in its neighbourhood.

Recently, Krabbe et al. (2014) estimated the electron density for a few H II regions in interacting galaxies, finding them to be systematically higher than those derived for H II regions belonging to isolated galaxies (taken from the literature). These authors found that the mean electron densities of star-forming regions in interacting galaxies are in the range $N_e = 24$–532 cm^{-3}, while those obtained for isolated galaxies are in the range $N_e = 40$–137 cm^{-3}. Our estimations of electron density for HCG 31A and HCG 31C are in the range for the interacting sample of Krabbe et al. (2014), which is consistent with the interaction scenario for HCG 31A+C.

For the first time, we report the detection of a super stellar cluster candidate, which could be evidence of current and triggered star formation in HCG 31A+C. In addition, unlike several studies that have been developed to understand the compact group HCG 31, the spatial resolution of the IFU observations allowed us to carry out a detailed analysis of different structures in the system HCG 31A+C. With this information, we estimated several physical properties of this system and we describe the star formation bursts in this region in more detail.

5.2 HCG 31 as a pre-merger object

Because of its complex morphology, several authors have suggested different scenarios to explain the origin of HCG 31. As mentioned earlier, Richer et al. (2003), using Fabry–Perot and spectroscopic data, suggest that galaxies HCG 31A and HCG 31C are a single entity. In contrast, Amram et al. (2007) used high-resolution Fabry–Perot data to suggest that both systems are independent late-type galaxies, in a pre-merger phase. This last scenario is also supported by the results presented in this paper.

In this context, the estimated SFRs can give us evidence for the merging scenario supported by Amram et al. (2007). Considering the area for the estimated SFR in the centre region, which corresponds to ~ 2.57 kpc^2, we obtain a star formation density of $\log \Sigma = 0.55$ M$_\odot$ yr^{-1} kpc^{-2} for SFR ~ 9.2 M$_\odot$ yr^{-1}. Although we do not have information about the quantity of atomic and molecular gas for HCG 31A+C, this star formation density locates this object in the upper region of the $\log \Sigma_{gas}$ versus $\log \Sigma_{SFR}$ plot presented by Daddi et al. (2010, fig. 2 in that paper). This suggests that HCG 31A+C is a strong starburst object. It will be difficult to reconcile this high star formation density with a single low-mass galaxy, therefore, these results support the scenario in which HCG 31 is a merging object and not a single entity.

5.3 Current and triggered star formation inside HCG 31A+C

In Sections 4.2 and 4.6, we suggest that there is a super stellar cluster located ~ 1 arcsec (270 pc) from the star formation burst associated with the galaxy HCG 31C. This super stellar cluster candidate has an intense stellar continuum emission, with respect to its vicinity. Besides, this object is spatially associated with a region with high velocity dispersions up to ~ 85 km s^{-1}. This suggests that the supercluster is cleaning its environment with an expanding shell, which should be produced by the strong stellar winds and/or the energy from supernovae events. The strong interactions of these winds and the environment seem to be triggering star formation
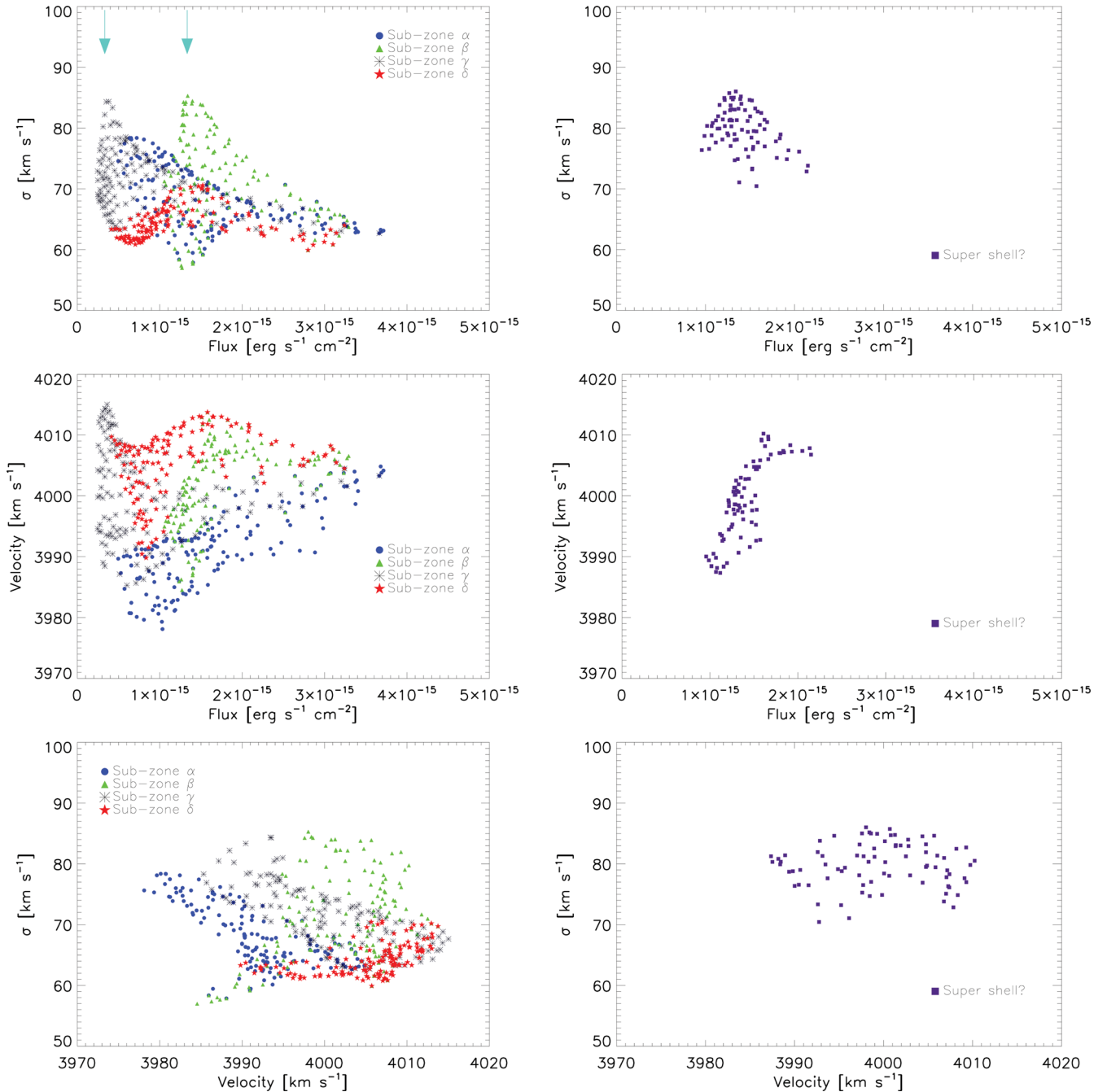
Figure 11. Top panels: σ versus flux diagram. Middle panels: Radial velocity versus flux diagram. Bottom panels: σ versus radial velocity diagram. The diagrams in the left column include the sub-zones in zone 4, α, β, γ and δ, which are represented as blue circles, green triangles, black asterisks and red stars, respectively. The diagrams in the right column include the points in the area in the fourth panel in Fig. 9 (purple square) represented by purple squares, which corresponds to the super shell produced by the possible super stellar cluster in sub-zone β (0.58 × 0.58 arcsec, 158 × 158 pc).

in its neighbourhood, since we can detect a strong Hα emission 270 pc away. To check if this scenario is possible, we estimated the velocity of the expanding bubble associated with the super stellar cluster, to determine if this quantity is in the range of expected values. Considering that the distance from the stellar cluster to the Hα peak is about ∼270 pc, and taking into account that the age of the complex is about 5 Myr (this work and López-Sánchez et al. 2004), we derived an expanding velocity of ∼53 km s^{-1}. This value is consistent with the expanding velocity of some giant H II regions

located in the Large Magellanic Cloud (LMC). For example, Rosado et al. (1996) measured an expanding velocity of 45 km s^{-1} in the central region of N11. Clearly, the star-forming complex in HCG 31 is much brighter than regions like N11 or even 30 Dor; however, this estimate does not contradict the scenario proposed above. In fact, triggered star formation has been found in local galaxies, like LMC, where it is possible to resolve individual stars (see the review by Elmegreen 2011 on this topic). Another widely studied region is NGC 604, in the spiral galaxy M33.

The proposed scenario for explaining the presence of the super stellar cluster candidate, which is triggering star formation in HCG 31C, is consistent with the one proposed by Tosaki et al. (2007) for the giant H II region NGC 604. These authors detected a high $CO(J = 3 - 2)/CO(J = 1 - 0)$ ratio for gas with an arclike distribution (called by the authors a 'high-ratio gas arc') around the stellar cluster of NGC 604. These authors proposed a relation between the *high-ratio gas arc*, the stellar cluster and the new stars in the Hα shell, suggesting the following scenario: in the first place, there would be what they called 'first-generation star formation' associated with the central stellar cluster. Then, by some common phenomena such as stellar winds and/or supernova explosions, there should be compression of the surrounding ISM, which would result in a dense gas layer with an arclike distribution (the *high-ratio gas arc*). Then, new stars would form within the dense gas layer, which they called 'second-generation star formation'. This is triggered by the stellar cluster (the first-generation stars). If this proposed scenario is correct, one could then observe this second star population in the mentioned dense gas layer in two ways, as shells emitting in Hα and compact radio continuum sources. Tosaki et al. (2007) mentioned that these facts suggest that the H II regions in the high-ratio gas arc are regions with current star formation, and the regions with past star formation corresponds to the central star cluster, which has dispersed the ISM around. The scenario proposed by Tosaki et al. (2007) for NGC 604 is supported by other authors (e.g., Martínez-Galarza et al. 2012, through the use of IR data). To confirm this scenario in the central region of HCG 31A+C, we would need new IR and CO information.

In addition, the scenario presented in this work is consistent with the two-stage starburst model proposed by Walborn & Parker (1992). In this model, there is a concentrated star-forming burst, which triggers a second burst after 2 Myr. This second generation of stars is formed in the molecular clouds located in the periphery of the primary star-forming burst, which would be caused by the energy from massive stars. We found a difference of 4 Myr between the super stellar cluster and the star-forming burst in HCG 31C, and considering the uncertainties, the scenario we suggest is consistent with this model. This star-forming mechanism is described by Elmegreen (1998), who called it 'large scale triggering: shells or rings'. In this mechanism, the ionized gas expansion triggers shell formation, which triggers star formation in its periphery. Elmegreen (1998) points out that the shell size depends on the pressure and environment density, and in low-density environments the shell can reach a size of a few hundred parsecs. These values are reached by the super shell, which we suggest is triggering star formation in HCG 31A+C ($\sim$300 pc).

6 CONCLUSIONS

For the first time, integral field spectroscopy data for the merging system HCG 31 is presented, specifically for HCG 31A+C. With all the data analysis and the different estimates of physical properties for this system, we suggest a triggered star formation scenario, and we propose there is a super stellar cluster candidate next to the star-forming burst associated with HCG 31C. The strong stellar winds associated with this source seem to be triggering a star formation event in its neighbourhood. Our data set supports the scenario that the central region of HCG 31 is a merger between two late-type spiral galaxies. This merger has triggered the star formation in the centre of HCG 31, namely, HCG 31A+C. The study we present in this paper shows the power of IFU data in analysing interactions in merging galaxies.

REFERENCES

Allende-Prieto C., Lambert D. L., Asplund M., 2001, ApJ, 556, 63
Allington-Smith J. et al., 2002, PASP, 114, 892
Amram P., Plana H., Mendes de Oliveira C., Balkowski C., Boulesteix J., 2003, A&A, 402, 865
Amram P. et al., 2004, ApJ, 612, L5
Amram P., Mendes de Oliveira C., Plana H., Balkowski C., Hernandez O., 2007, A&A, 471, 753
Baldwin J. A., Phillips M. M., Terlevich R., 1981, PASP, 93
Barbá R. H., Rubio M., Roth M. R., García J., 2003, AJ, 125, 19
Barbá R. H., Maíz Apellániz J., Pérez E., Rubio M., Bolatto A., Fariña C., Bosch G., Walborn N. R., 2009, Ap&SS, 324, 309
Bordalo V., Plana H., Telles E., 2009, ApJ, 696, 1668
Calzetti D., Armus L., Bohlin R. C., Kinney A. L., Koornneef J., Storchi-Bergmann T., 2000, ApJ, 533, 682
Cedrés B., Cepa J., Tomita A., 2005, ApJ, 634, 1043
Cid Fernandes R., Stasińska G., Schlickmann M., Mateus A., Asari N. V., Schoenell W., Sodré L., 2010, MNRAS, 403, 1036
Daddi E. et al., 2010, ApJ, 714, L118
De Robertis M. M., Dufour R. J., Hunt R. W., 1987, J. Roy. Astron. Soc. Canada, 81, 195
Domínguez A. et al., 2013, ApJ, 763, 145
Elmegreen B. G., 1998, in Woodward C. E., Shull J. M., Thronson H. A., Jr, eds, ASP Conf. Ser. Vol. 148, Origins. Astron. Soc. Pac., San Francisco, p. 150
Elmegreen B. G., 2011, in Charbonnel C., Montmerle T., eds, EAS Publ. Ser. Vol. 51, Star Formation in the Local Universe. Cambridge Univ. Press, Cambridge
Eufrasio R. T., Dwek E., Arendt R. G., de Mello D. F., Gadotti D. A., Urrutia-Viscarra F., Mendes de Oliveira C., Benford D. J., 2014, ApJ, 795, 89
Fariña C., Bosch G. L., Barbá R. H., 2012, AJ, 143, 43
Fiorentino G. et al., 2012, Ap&SS, 341, 143
Fitzpatrick E. L., 1999, PASP, 111, 63
Gallagher S. C. et al., 2010, AJ, 139, 545
Hickson P., 1982, ApJ, 255, 382
Hickson P., Mendes de Oliveira C., Huchra J. P., Palumbo G. G., 1992, ApJ, 399, 353
Hook I. M., Jorgensen I., Allington-Smith J. R., Davies R. L., Metcalfe N., Murowinski R. G., Crampton D., 2004, PASP, 116, 425
Iglesias-Páramo J., Vilchez J. M., 1997, ApJ, 479, 190
Iglesias-Páramo J. et al., 2006, ApJSS, 164, 38
Johnson K. E., Conti P. S., 2000, AJ, 119, 2146
Kauffmann G. et al., 2003, MNRAS, 346, 1055
Kennicutt R. C., Jr, 1998, ARA&A, 36, 189

Kewley L. J., Dopita M. A., Sutherland R. S., Heisler C. A., Trevena J., 2001, ApJ, 556, 121

Krabbe A. C., Rosa D. A., Dors O. L., Pastoriza M. G., Winge C., Hägele G. F., Cardaci M. V., Rodrigues I., 2014, MNRAS, 437, 1155

Leitherer C., Heckman T. M., 1995, ApJS, 96, 9

Leitherer C., Schaerer D., Goldader J. D. et al., 1999, ApJS, 123, 3

López L. A., Krumholz M. R., Bolatto A. D., Prochaska J. X., Ramirez-Ruiz E., Castro D., 2014, ApJ, 795, 121

López-Sánchez A. R., Esteban C., Rodríguez M., 2004, ApJS, 153, 243

Maíz-Apellániz J., Pérez E., Mas-Hesse J. M., 2004, AJ, 128, 1196

Marino R. A. et al., 2013, A&A, 559A, 114

Martínez-Delgado I., Tenorio-Tagle G., Muñoz-Tuñón C., Moiseev A. V., Cairós L. M., 2007, AJ, 133, 2892

Martínez-Galarza J. R., Hunter D., Groves B., Brandl B., 2012, ApJ, 761, 3

Mendes de Oliveira C. L., Temporin S., Cypriano E. S., Plana H., Amram P., Sodré L. J., Balkowski C., 2006, AJ, 132, 570

Moiseev A. V., Lozinskaya T. A., 2012, MNRAS, 423, 1831

Muñoz-Tuñón C., Tenorio-Tagle G., Castañeda H. O., Terlevich R., 1996, AJ, 112, 1636

Osterbrock D. E., 1989, Astrophysics of Gaseous Nebulae and Active Galactic Nuclei. University Science Books, Mill Valley, CA

Perez J., Michel-Dansac L., Tissera P. B., 2011, MNRAS, 417, 580

Plana H., Amram P., Mendes de Oliveira C., Balkowski C., Boulesteix J., 2003, AJ, 125, 1736

Richer M. G., Georgiev L., Rosado M., Bullejos A., Valdez-Gutiérrez M., Dultzin-Hacyan D., 2003, A&A, 397, 99

Rosado M., Laval A., Le Coarer E., Georgelin Y. P., Amram P., Marcelin M., Goldes G., Gach J. L., 1996, A&A, 308, 588

Rubin V. C., Hunter D. A., Ford W. K. J., 1990, ApJ, 365, 86

Rupke D. S. N., Kewley L. J., Barnes J. E., 2010, ApJ, 710, L156

Sánchez S. F. et al., 2012, A&A, 538, A8

Stasińska G., Cid Fernandes R., Mateus A., Sodré L., Asari N. V., 2006, MNRAS, 371, 972

Torres-Flores S., Mendes de Oliveira C., Amram P., Alfaro-Cuello M., Carrasco E. R., de Mello D. F., 2015, ApJ, 798, L24

Tosaki T., Miura R., Sawada T., Kuno N., Nakanishi K., Kohno K., Okumura S. K., Kawabe R., 2007, ApJ, 664, L27

Verdes-Monetengro L., Del Olmo A., Yun M. S., Perea J., 2005, A&A, 430, 443

Vilchez J. M., Iglesias-Páramo J., 1998, ApJ, 508, 248

Walborn N. R., Parker J. W., 1992, ApJ, 399, L87

Williams B. A., McMahon P. M., van Gorkom J. H., 1991, AJ, 101, 1957

This paper has been typeset from a TEX/LATEX file prepared by the author.